AGU
ADVANCING
EARTH AND
SPACE SCIENCE

Geophysical Research Letters®

Key Points:

- Superrotation of the thermosphere exhibits large longitudinal and seasonal variations
- Geomagnetic field geometry and lower atmospheric tides are vital for the longitudinal patterns of superrotation
- Viscous force also partly contributes to the longitudinal variation in superrotation

Correspondence to:
H. Wang,
h.wang@whu.edu.cn

Longitudinal Variation in the Thermospheric Superrotation: CHAMP Observation and TIE-GCM Simulation

Hui Wang[1] , **H. Lühr[2]** , and **K. D. Zhang[1]**

[1]Department of Space Physics, School of Electronic Information, Wuhan University, Wuhan, China, [2]German Research Center for Geosciences, GFZ, Section 2.3, Geomagnetism, Potsdam, Germany

Abstract By means of 4 years of Challenging Minisatellite Payload (CHAMP) zonal wind observations and a Thermosphere-Ionosphere Electrodynamics General Circulation Model simulation, longitudinal and seasonal variations of thermospheric superrotation at magnetic equator are investigated first. The superrotation shows four- and three-peaked longitudinal patterns in March and September equinoxes, and a two-peaked variation during solstices. The superrotation is stronger in December than in June solstice, and stronger in March than in September equinox. The mean correlation between the zonal variation of superrotation and nighttime eastward wind is about 0.8, while it is 0.6 with daytime westward zonal wind. The interaction between the neutral wind and geomagnetic field plays a more important role in the superrotation, rather than the F-region electron density. The lower atmospheric tides tend to suppress the superrotation, but contribute to the longitudinal patterns of the superrotation. The viscous force is also important for the longitudinal modulation of the superrotation.

Plain Language Summary The low altitude atmosphere rotates together with the Earth, resulting from the friction with the surface. Owing to the high viscosity, most parts of the atmosphere at different altitudes also rotate at the same rate as the Earth. Above 200 km, however, the low-latitude atmosphere is found to rotate 10%–20% faster than the Earth. This phenomenon is more prominent on Venus, where the atmospheric circulation speed can reach 60 times of the rotation. Although this unexpected superrotation phenomenon was discovered in the 1960s in connection with satellite orbit evaluations, its physical mechanism has not been fully elucidated to date. This study reveals for the first time that the geomagnetic field configuration and the lower atmospheric tides have important effects on the superrotation of the upper atmosphere. Both can account for the longitudinal variation in the superrotation. This theoretical study is helpful for better understanding the generation mechanism of the superrotation on Earth and other planets.

1. Introduction

At low latitudes, the day-night temperature differences due to the solar irradiation causes a pressure gradient that is directed from noon to midnight. This drives the westward zonal wind during daytime and eastward wind at night. A fast zonal wind jet band is found along the magnetic equator, rather than along the geographic equator because of the reduced ion drag effect (Liu et al., 2009). Superrotation occurs when the daily average zonal wind in the thermosphere exceeds the Earth's rotational speed, and it has measurable effects on inclination changes of the satellite orbital plane.

The first superrotation study was conducted by King-Hele (1964), who interpreted satellite drag data and reported that the rotation of the atmosphere was 20% faster than that of the Earth. Using Dynamic Explorer 2 (DE2) satellite observations during 1981 and 1982, Wharton et al. (1984) then reported that the equatorial zonal wind velocity exceeded the Earth's rotation by ~18 m/s at an altitude between 200 and 700 km, and Coley and Heelis (1989) found that superrotation attained a peak at the magnetic equator. Using Challenging Minisatellite Payload (CHAMP) zonal wind data from 2002 to 2004, Liu et al. (2006) revealed that the superrotation increased from 22 m/s at the solar medium (F10.7 = 100 sfu) to 63 m/s at the solar maximum (F10.7 = 190 sfu) because the eastward wind increased with the enhanced solar activity, whereas the westward wind decreased in velocity. Rishbeth (2002) reported a superrotation velocity of 47 m/s at an altitude of 400 km from a Thermosphere-Ionosphere Electrodynamics General Circulation

Model (TIE-GCM) simulation. The study of Tao et al. (2017) analyzed Ground-to-topside model of Atmosphere and Ionosphere for Aeronomy (GAIA) simulations and determined that a superrotation velocity of 53.3 m/s existed above an altitude of 200 km when F10.7 was between 170 and 230 sfu. However, when the geomagnetic field was reduced artificially by 90%, the resulting superrotation decreased to 43 m/s, and the authors explained that the reduced magnetic field increased the ion drag, thus reducing the eastward wind.

The superrotation of the thermosphere is generally explained by the E- to F-layer electromagnetic coupling process (for more information see the comprehensive review by Rishbeth, 2002). The daytime plasma drifts are controlled mostly by the E-region dynamo electric field, whereas the F-region dynamo becomes more important at nighttime. The F-region dynamo electric field drives the eastward plasma drift to become as large as the eastward wind, and the ion drag at night is thus reduced, whereas the eastward wind is enhanced. In addition, the nighttime electron density (Ne) is much lower than that during daytime, which causes the nighttime ion drag to be reduced to a level lower than that of the daytime, thus facilitating the fast eastward winds (Pacheco et al., 2011). The prereversal enhancement of the eastward electric field also contributes to superrotation by uplifting the F-layer peak of the ionosphere, which consequently leads to a lower electron density and ion drag in the F-region, and thus enhances the eastward wind at night (Anderson & Roble, 1974).

However, it is currently unclear how the superrotation of the atmosphere varies with longitude. In this study, 4 years (2002–2005) of zonal wind observations from the CHAMP satellite were analyzed, and the prominent longitudinal difference in the superrotation of the atmosphere and its seasonal dependence was determined. In addition, a TIE-GCM model simulation was conducted to discuss the physical mechanism involved.

2. Data and Model

The CHAMP satellite was launched in 2000 with an orbital inclination of 87.3° and an initial altitude of approximately 450 km (Reigber et al., 2002); it then dropped to an average altitude of ~400 km during 2002 and 2005. CHAMP carried a sensitive accelerometer, from which the neutral zonal wind can be retrieved at an accuracy of ~±10 m/s and at a temporal resolution of 10 s (Doornbos et al., 2010). 15 s electron density samples are obtained using a planar Langmuir probe, and the quasi-dipole coordinates, as described by Richmond (1995), are used to define the geomagnetic latitude. The CHAMP orbit processed through all local times in approximately 130 days. In this study, to cover a period of 24 h local time, the data were examined in sets of 131 days centered on the March equinox, June solstice, September equinox, and December solstice days.

TIE-GCM is a three-dimensional model of the coupled thermosphere and ionosphere, in which the driving forces are the high-latitude convection electric field, solar extreme ultraviolet, and ultraviolet spectral fluxes, which are represented by the F10.7 index, and the diurnal and by semidiurnal low atmospheric tides, which are obtained from a global scale wave model (Hagan & Forbes, 2002; Heelis et al., 1982; Weimer, 2005). The horizontal resolution of TIE-GCM is 2.5° in geographic latitude (GLat) and longitude (GLon), and the altitude ranges from ~97 to ~700 km. In this study, the model was run for 20 days to reach a steady state, and the outputs of the one-day data were used for the following theoretical study. The input parameters of the model during a quiet period at solar maximum were as follows: a hemispheric power of auroral precipitation of 18 GW, a cross polar cap potential of 30 kV, and an F10.7 of 170 sfu.

3. Results

Figure 1 (left side) shows the distribution of the diurnal (24 h) average zonal wind (i.e., superrotation) in the frame of geomagnetic latitude (MLat) and geographic longitude for four seasons during magnetically quiet periods (Kp < 3). Note that the data were examined in sets of 131 days, combining the seasons from the four years. The data were sorted into longitudinal bins of 30° and latitudinal bins of 10°. It can be seen that superrotation is prominent near the magnetic equator. At equinoxes, the superrotation maximizes at the magnetic equator, it decreases toward higher latitudes, and it turns to subrotation at latitudes higher than 20° (see the red and black curves in Figure 1, right panel). At solstices, the superrotation is strong at
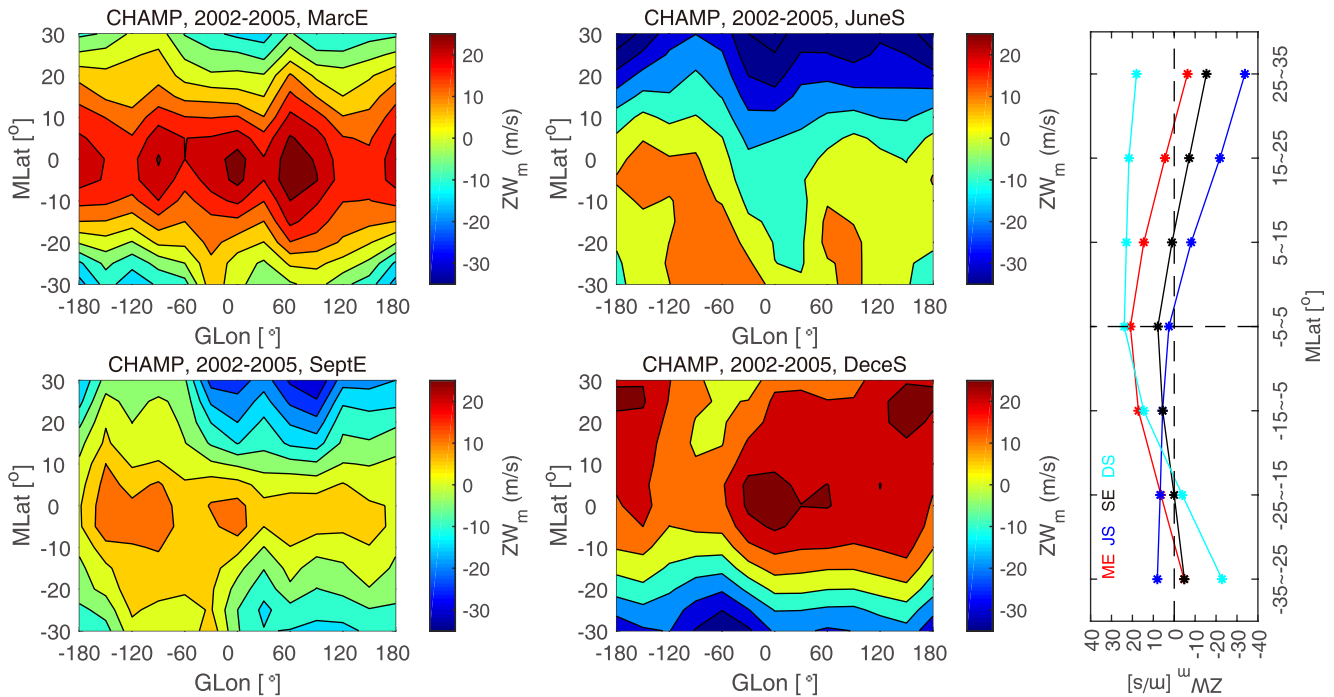
Figure 1. The 131-day mean Challenging Minisatellite Payload (CHAMP) zonal wind observations, centered around the four seasons. (Left) Geographic longitude versus magnetic latitude distribution of the mean diurnal zonal wind from the years 2002–2005, separated by season. (Right) The zonal wind, averaged over longitude, as a function of MLat.

the equator and at midlatitudes in the winter hemisphere, and it decreases rapidly with increasing latitude toward the summer hemisphere (blue and cyan curves). The superrotation is strongest around December solstice (23.9 m/s) and weakest at the June solstice (7.8 m/s), and its value is greater during the March equinox and during the September equinox (21.0 m/s and 8.1 m/s). It is of interest that the superrotation shows obvious longitudinal variations near the magnetic equator, and these vary with the season. A wave-4 structure appears around March equinox, a wave-3 structure at the September equinox, and a wave-2 structure at the June and December solstices.

The longitudinal variation in the diurnal mean zonal wind within the equatorial region ($\pm5°$MLat) is shown in Figure 2a (left column). Four peaks are located at $-180°$, $-90°$, $0°$, $60°$ GLon around March equinox, with a maximum value of 27.3 m/s appearing at 60° GLon. The peak values of the wave-3 pattern at September equinox appear at $-120°$, $-30°$, and 120° GLon, of which $-120°$ is the strongest (13.1 m/s). The zonal changes in the June and December solstices are almost opposite in phase. Around June solstice, the superrotation in the western hemisphere is higher than that in the eastern hemisphere, with a peak located at $-150°$GLon (12.4 m/s), and this situation is reversed at December solstice, with a peak value near 0°GLon (32.8 m/s).

Superrotation is the diurnal average of the daytime westward wind and nighttime eastward wind. With the aim of determining which component is more important for the longitudinal variation of the superrotation, Figure 2a (middle and right columns) illustrates the longitudinal distribution of the neutral wind pattern during daytime (06:00–16:00 MLT) and nighttime (18:00–04:00 MLT), respectively. Note that these are 131-day means centered at the solstice/equinox days. These day and nighttime zonal wind structures are consistent with the results of Häusler et al. (2007), and they show four peaked longitudinal variations at the equinoxes, with maxima at ∼09:00 and 21:00 MLT. The wind phase is opposite in these two local time sectors. Häusler and Lühr (2009) revealed the full spectrum of nonmigrating tides in the upper thermosphere using CHAMP observation. Future work can study the wave coupling in details using TIE-GCM. The correlation coefficients between the average diurnal zonal winds (i.e., superrotation) and the daytime (nighttime) average zonal winds are listed in the corresponding subfigures. It is evident that the correlation is reasonably good in all cases (except for the westward wind during the June solstice). However, it is
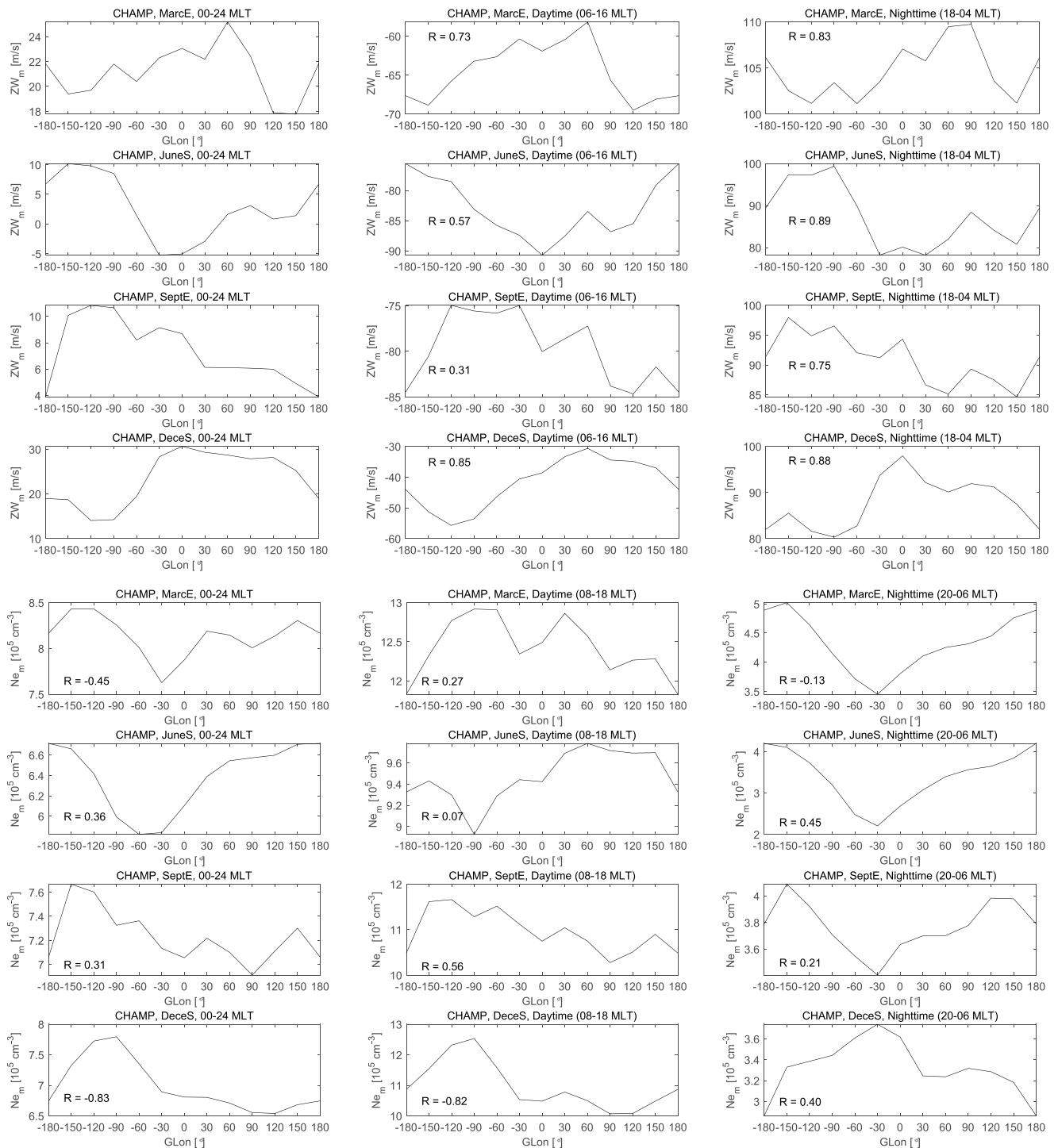
Figure 2. (a) The geographic longitudinal variations of the diurnal (left column), daytime (middle column) and nighttime (right column) low-latitude mean zonal wind. From top to bottom are shown: Mach equinox, June solstice, September equinox, and December solstice. These are 131-day means centered around the solstices/equinoxes. The correlation coefficients between the average diurnal zonal winds (i.e., superrotation) and the daytime (nighttime) average zonal winds are listed in the corresponding subfigures. (b) The same format as the top panel, but for the electron density (*Ne*). The correlation coefficients between the zonal winds (i.e., superrotation) and *Ne* variations are listed in the corresponding *Ne* frames.

obvious that superrotation generally correlates better with the eastward wind than with the westward wind, which indicates that the eastward wind on the nightside plays a more important role in the longitudinal change of superrotation. This is the first study to distinguish the relative contributions of daytime westward and nighttime eastward winds to the longitudinal variation of superrotation. For the E-F layer coupling, the daytime is dominated by the E-region dynamo, and the nighttime is dominated by the F-region dynamo. The correlation study conducted in this way allows a rather rough division of the contributions made by E or F dynamo. The results show that the zonal difference of the diurnal averaged eastward wind is most strongly influenced by the nighttime F dynamo process.

According to previous studies, superrotation is related to ion drag in the F-layer at night (Rishbeth, 2002), and the ion drag is proportional to the product of the electron density and the difference in the neutral-ion velocity. Figure 2b shows the distribution of the electron density (Ne) at the magnetic equator ($\pm 5°$MLat) over longitude, as measured by the CHAMP satellite, in the same format as that given in Figure 2a. In the case of Ne, the day/night local time boundaries are shifted by two hours (later). Stolle et al. (2008) showed that Ne responds at an altitude of 400 km, ~ 2 h after changes in the E-region dynamo take place. It is clearly evident that the tidal characteristics of Ne differ between day and night. This was previously reported by Xiong et al. (2014), and this is caused by a change in coupling between the E- and F-regions. The correlation coefficients between the electron density and zonal wind are listed in each subfigure for each season and separately for the whole day, daytime, and nighttime, and it can be seen that the correlation between the zonal wind and Ne is not well except for the December solstice when the anti-correlation with Ne is strong during the daytime. This highlights that the ion density effect is prominent in winter.

By assuming that ionospheric electron density (conductivity) plays an important role in superrotation, Rishbeth (2002) predicted that superrotation would be higher in the spring than in the autumn, and higher in India than in South America. This hypothesis can be partly (but not completely) confirmed by the CHAMP observations, as the superrotation in March is stronger than that in the September equinox, and the December superrotation is higher than the June solstice (as shown in Figure 1. Such a solstice difference is consistent with the results of Liu et al., 2006). However, the CHAMP observations also show that although the superrotation is higher in the Indian sector than in the South American sector during the March equinox and December solstice, the reverse situation is true for the September equinox and June solstice.

The magnitude of the superrotation is sensitive to the intensity of the F10.7 flux. The average F10.7 is examined over the same time span as the data used for CHAMP, which is 132, 126, 125, and 122 sfu for March, June, September, and December, respectively. The variation of equinoxes is partly due to seasonal variation of F10.7 flux. However, the difference between summer and winter solstices cannot be explained by F10.7 flux. A possibility of weaker superrotation at June solstice could be related to the frequently observed weak pre-reversal enhancement of the electric field (PRE) in June. The eastward wind jet in the evening is related to the equatorial ionization anomaly, which is due to PRE (Liu et al., 2009). It is known that PRE is strong around equinox and December, but weak around June (Fejer et al., 2008). Moreover, the westward wind at daytime is weaker in December than in June. This can be related to the larger electron density in December than in June (see Figure 2b, middle column), which is known as the winter anomaly. The larger ion drag at daytime in December can suppress the westward wind. Both processes could explain the larger superrotation in December than in June.

Previous studies mainly focused on the relationship between superrotation and ion drag in the F-layer at night (e.g., Rishbeth, 2002). CHAMP provided in situ measurements of electron density and zonal wind, thus, it provides a good opportunity to verify the direct relationship between ion density and superrotation. The weak correlation between Ne and superrotation at equinox and June Solstice indicates the importance of physical processes other than ion density. The ion drag is proportional to the product of the ion density and the difference in the neutral-ion velocity. Therefore, the combined effect of velocity difference and ion density may be more important for superrotation than the ion density itself. In addition, the neutral wind is controlled by the balance between pressure gradient, ion drag, Coriolis, and viscous force. The effects of these forces can be distinguished by using a physical model.
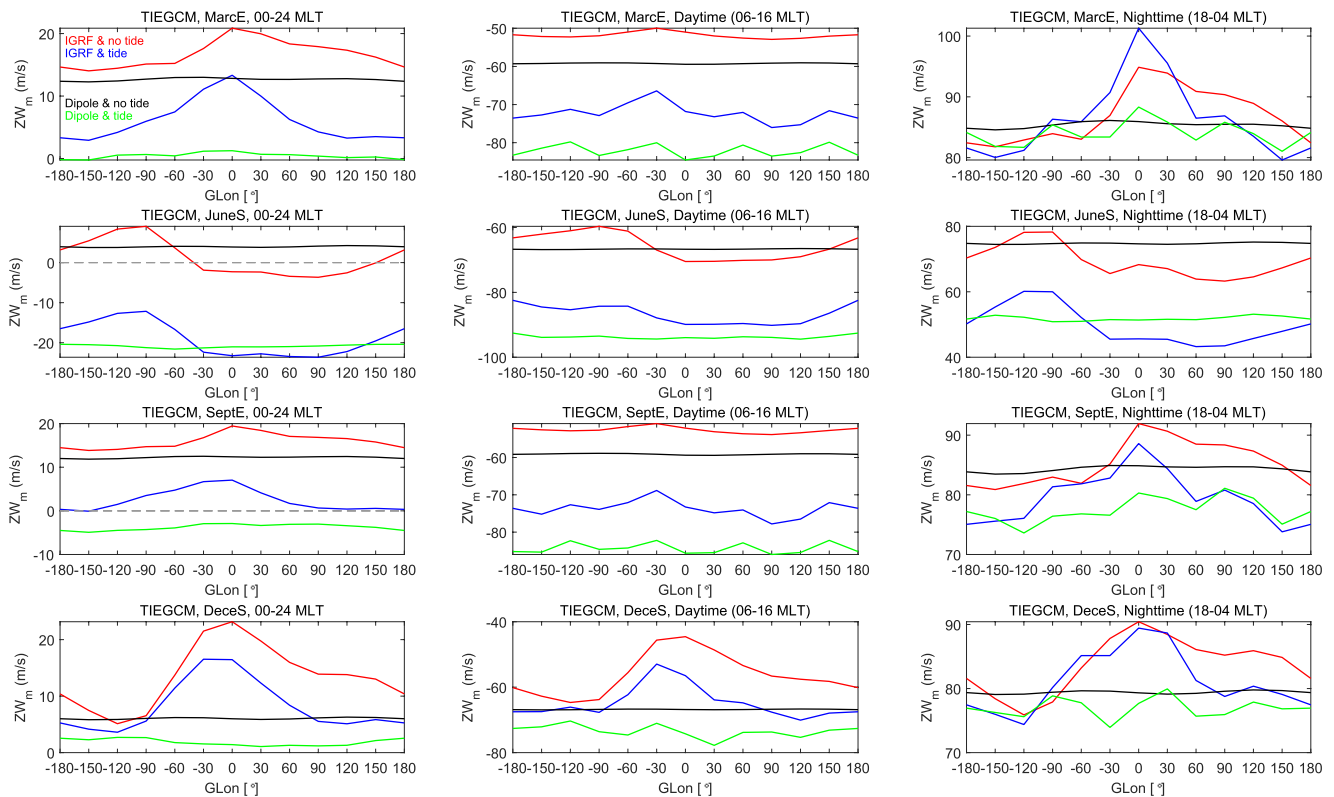
Figure 3. Zonal wind variations at magnetic equator over geographic longitudinal of the average diurnal (left), or the daytime (middle) and nighttime (right) velocities, as simulated by Thermosphere-Ionosphere Electrodynamics General Circulation Model (TIE-GCM). The red (blue) curve represents the runs considering the IGRF and without (with) tidal input at the low boundary of the model. The black (green) curve represents the cases using only a centered dipole and without (with) tidal input. From top to bottom are shown March equinox, June solstice, September equinox, and December solstice.

4. Discussion

The TIE-GCM model was used to study the physical mechanisms responsible for the longitudinal variation of the superrotation. For each season four cases were examined: with/without migrating and nonmigrating tidal forcing when considering the IGRF geomagnetic field configuration, and with/without tidal forcing by assuming a centered dipole magnetic field where the geomagnetic axis coincides with the rotation axis. By comparing these cases, the effects of the tides and geomagnetic field geometry on the longitudinal variation of the superrotation was evaluated. The simulation results are depicted in Figure 3, and they are presented in the same format as those in Figure 2a. Note that TIE-GCM results were not sampled along CHAMP tracks. In the ideal simulation, F10.7 is set to 170 sfu, which is larger than the observed value during the CHAMP period. This is because the TIE-GCM underestimates the neutral wind (Wang & Lühr, 2016). Tao et al. (2017) found that the GAIA could reproduce obvious superrotation when the F10.7 index was set to be 170–230 sfu, and that it could not reproduce the superrotation when F10.7 was low. The superrotation value at March equinox presented by Rishbeth (2002) was based on TIE-GCM, when F10.7 was set to even higher values, 215 and 243 sfu (Richmond et al., 1992).

The underestimation of the neutral wind pattern by physical models is a known fact (e.g., Deng & Ridley, 2006; Wang & Lühr, 2016; Zhang et al., 2018). A possible reason is related to the model resolution, which may affect the magnitude of outputs. The horizontal resolution of TIE-GCM is 2.5° in geographic latitude (GLat), while it is 0.6° at GLat for CHAMP samples. This means, the model can only reproduce large-scale structure, as expected, it is weaker than relatively fine-scale observation. Deng and Ridley (2006) found that when the latitudinal resolution was changed from 5° to 1.5° in GITM, the neutral gas heating rate could increase by 20% because the model could better capture small-scale electric field and particle precipitation. Another factor is that TIE-GCM is based, for high-latitude electric fields, on the empirical Heelis model, which only predicts the average state of the high-latitude ion convection for a given 3-hourly Kp index. The

real geomagnetic activity changes more rapidly with time, potentially causing differences between model predictions and satellite observations. Nevertheless, previous studies have reported that there is a large degree of similarity between simulations and observations from ground- and space-based equipments (e.g., W. B. Wang et al., 2012; Wu et al., 2019).

It can be seen that in the case of a central dipole magnetic field, the longitudinal variation in the average wind is negligible (see the black and green curves). This is caused by the invariant magnetic field along longitudes for a centered dipole. Conversely, when the IGRF field is considered, there are obvious longitudinal variations (red and blue curves). These results indicate that the geomagnetic field configuration is the main reason for the longitudinal variation of superrotation. In addition, it is evident that the tides, which are excited in the low atmosphere, tend to suppress the superrotation, and this is true for both the IGRF and central dipole field cases (as shown by a comparison between the blue/cyan curves and the red/blue curves). There have been no previous reports confirming that tides tend to suppress superrotation. The underlying reason may be that the subrotation (westward wind) is dominant at low altitudes. Subsequently, the superrotation at higher altitudes can be retarded by adding the low atmospheric forcing (i.e., tides).

When compared to the CHAMP observations in Figure 2, it can be seen that for the condition with IGRF and without a tidal input (red curve), the TIE-GCM basically reproduces the principal longitudinal structures of the superrotation at solstices. When the low atmospheric tidal input is imposed, it also includes certain planetary waves, Kelvin waves, and secondary waves due to their nonlinear interactions. At equinoxes, the model reproduces a single peak around 0° GLon, but it does not show the other three peaks. At September equinox the peak at −90°GLon is still visible, but it is not obvious around March equinox. As shown in Figure 3, with a tidal input the nighttime eastward wind at March equinox also shows peaks at −180°, −90°, and 90°GLon, but they are clearly weaker than the peak at 0° GLon. Therefore, TIE-GCM appears to underestimate the atmospheric tidal effects in the equatorial region. This result is consistent with previous results. For example, H. Wang et al. (2020) used both CHAMP satellite observations and TIE-GCM simulations to study the longitudinal structure of the equatorial electrojet and found that TIE-GCM underestimated the tidal wave effect in East Asia. This is at least partly due to the insufficient lower boundary forcing in these zones, as well as inaccuracies in the tidal dissipation scheme of the TIE-GCM. In addition, Häusler et al. (2010) compared the tidal signals in the zonal wind, as observed by CHAMP, and the output by the thermosphere-ionosphere-mesosphere-electrodynamics general circulation model (TIME-GCM) and found that TIME-GCM simulations were not able to correctly reproduce the intraannual variations of the eastward-propagating diurnal tide with zonal wavenumber 3 (DE3), which is evident as a wave-4 structure.

To reveal the physical mechanism causing the longitudinal modulation of the superrotation, we conducted a term analysis of the upper atmospheric superrotation. The zonal wind is primarily driven by a balance between the pressure gradient, ion drag, Coriolis, and viscous force (Hsu et al., 2016; H. Wang et al., 2017; Zhang et al., 2018). Figure 4 illustrates the diurnally averaged acceleration terms of these forces at magnetic equator as a function of GLon. It can be seen that during equinoxes the ion drag (blue curve) acts as an impeding force on the superrotation, the viscous force (black curve) largely balances the ion drag, and the longitudinal variation of the pressure gradient (red curve) is negligible. However, around the solstices, both the pressure gradient and viscous force vary nearly in anti-phase with the ion drag. An interesting feature is that the viscous force contributes significantly to the modeled longitudinal variation of superrotation in all seasons (compare Figure 3 and Figure 4). The effect of the Coriolis force on superrotation at equinoxes can be ignored (green curve), but it makes some contributions during solstices, especially at around −90° GLon.

In summary, the results show obvious longitudinal and seasonal variations of the superrotation velocity in the magnetic equatorial region. The zonal wind variations associated with the superrotation are better correlated with the nighttime eastward wind (correlation coefficient R of annual average is about 0.8) than with the westward wind during the daytime (R is about 0.6). The superrotation velocity is larger around December than at the June solstice, and higher around March equinox than at September equinox. Wave-4 longitudinal variations are observed in March, wave-3 variations in September, and wave-2 variations around the solstices. It is also evident that the longitudinal dependence of the viscous force has a supporting effect on superrotation and that the interaction between the wind and the geomagnetic field configuration
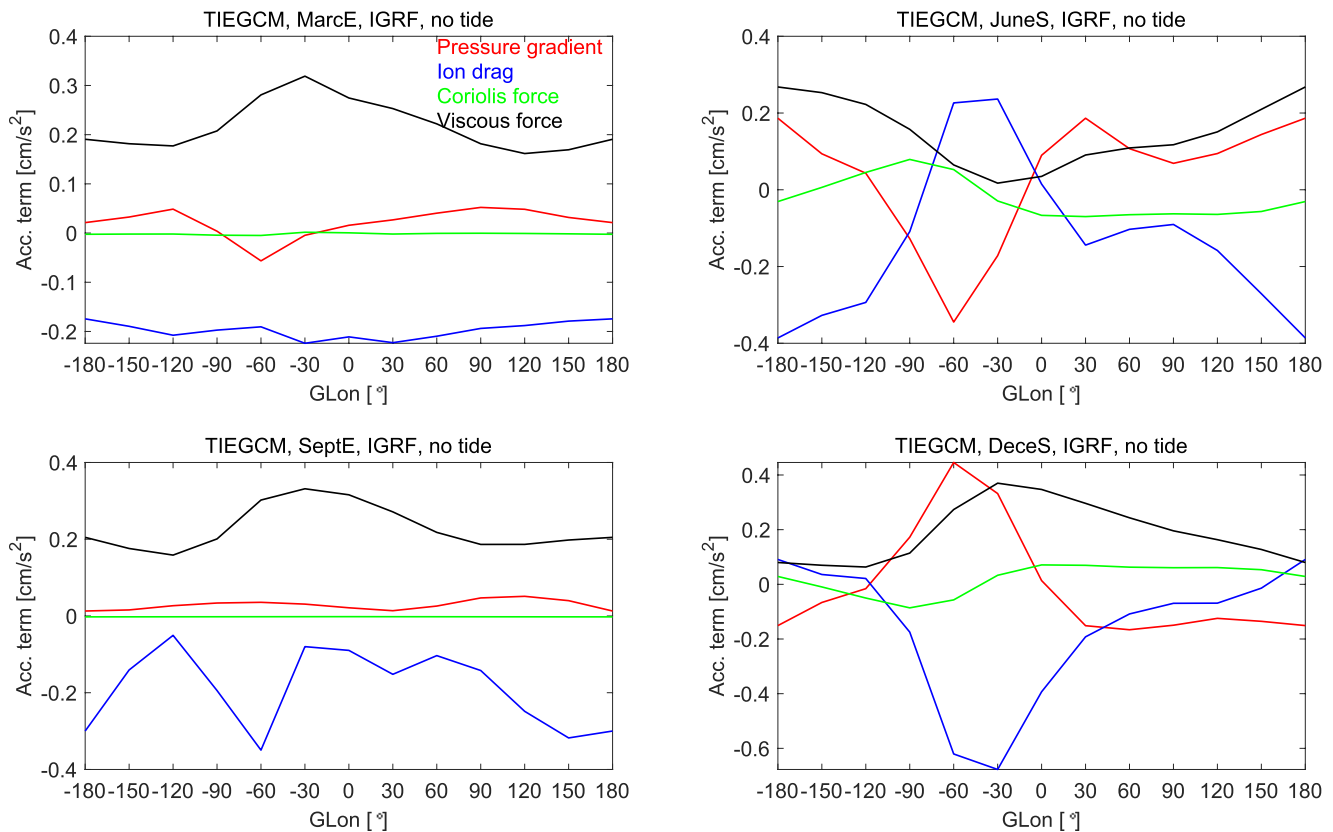
Figure 4. The effects of main acceleration terms on the zonal wind, such as pressure gradient, ion drag, Coriolis and Viscous forces (represented by different colors), have been simulated for the case with IGRF but without tides, separately for all four seasons.

plays a more important role for the actual superrotation of the terrestrial thermosphere than the F-region electron density.

Data Availability Statement

References

Anderson, D. N., & Roble, R. G. (1974). The effect of vertical E×B ionospheric drifts of F region neutral winds in the low-latitude thermosphere. *Journal of Geophysical Research*, *79*, 5231–5236. https://doi.org/10.1029/ja079i034p05231

Coley, W. R., & Heelis, R. A. (1989). Low-latitude zonal and vertical ion drifts seen by DE 2. *Journal of Geophysical Research*, *94*(A6), 6751–6761. https://doi.org/10.1029/ja094ia06p06751

Deng, Y., & Ridley, A. J. (2006). Dependence of neutral winds on convection E-field, solar EUV, and auroral particle precipitation at high latitudes. *Journal of Geophysical Research*, *111*, A09306. https://doi.org/10.1029/2005JA011368

Doornbos, E., van den IJssel, J., Lühr, H., Forster, M., & Koppenwallner, G. (2010). Neutral Density and Crosswind Determination from Arbitrarily Oriented Multiaxis Accelerometers on Satellites. *Journal of Spacecraft and Rockets*, *47*(4), 580–589. https://doi.org/10.2514/1.48114

Fejer, B. G., Jensen, J. W., & Su, S. Y. (2008). Quiet time equatorial F region vertical plasma drift model derived from ROCSAT-1 observations. *Journal of Geophysical Research*, *113*, A05304. https://doi.org/10.1029/2007JA012801

Hagan, M. E., & Forbes, J. M. (2002). Migrating and nonmigrating diurnal tides in the middle and upper atmosphere excited by tropospheric latent heat release. *Journal of Geophysical Research*, *107*(D24). https://doi.org/10.1029/2001jd001236

Häusler, K., & Lühr, H. (2009). Nonmigrating tidal signals in the upper thermospheric zonal wind at equatorial latitudes as observed by CHAMP. *Annales Geophysicae*, *27*, 2643–2652. https://doi.org/10.5194/angeo-27-2643-2009

Häusler, K., Lühr, H., Hagan, M. E., Maute, A., & Roble, R. G. (2010). Comparison of CHAMP and TIME-GCM nonmigrating tidal signals in the thermospheric zonal wind. *Journal of Geophysical Research*, *115*, D00I08. https://doi.org/10.1029/2009JD012394

Häusler, K., Lühr, H., Rentz, S., & Köhler, W. (2007). A statistical analysis of longitudinal dependences of upper thermospheric zonal winds at dip equator latitudes derived from CHAMP. *Journal of Atmospheric and Solar-Terrestrial Physics*, *69*(12), 1419–1430. https://doi.org/10.1016/j.jastp.2007.04.004

Heelis, R. A., Lowell, J. K., & Spiro, R. W. (1982). A model of the high-latitude ionospheric convection pattern. *Journal of Geophysical Research*, *87*(A8), 6339–6345. https://doi.org/10.1029/ja087ia08p06339

Hsu, V. W., Thayer, J. P., Wang, W., & Burns, A. (2016). New insights into the complex interplay between drag forces and its thermospheric consequences. *Journal of Geophysical Research*, *121*(10417–10), 430. https://doi.org/10.1002/2016ja023058

King-Hele, D. G. (1964). The rotational speed of the upper atmosphere determined from changes in satellite orbits. *Planetary and Space Science*, *12*(9), 835–853. https://doi.org/10.1016/0032-0633(64)90044-3

Liu, H., Lühr, H., Watanabe, S., Köhler, W., Henize, V., & Visser, P. (2006). Zonal winds in the equatorial upper thermosphere: Decomposing the solar flux, geomagnetic activity, and seasonal dependencies. *Journal of Geophysical Research*, *111*(A7), A07307. https://doi.org/10.1029/2005JA011415

Liu, H., Watanabe, S., & Kondo, T. (2009). Fast thermospheric wind jet at the Earth's dip equator. *Geophysical Research Letters*, *36*(8), L08103. https://doi.org/10.1029/2009GL037377

Pacheco, E. E., Heelis, R. A., & Su, S.-Y. (2011). Superrotation of the ionosphere and quiet time zonal ion drifts at low and middle latitudes observed by Republic of China Satellite-1 (ROCSAT-1). *Journal of Geophysical Research*, *116*, A11329. https://doi.org/10.1029/2011JA016786

Reigber, C., Lühr, H., & Schwintzer, P. (2002). CHAMP mission status. *Advances in Space Research*, *30*(2), 129–134. https://doi.org/10.1016/s0273-1177(02)00276-4

Richmond, A. D. (1995). Ionospheric electrodynamics using magnetic apex coordinates. *Journal of Geomagnetism and Geoelectricity*, *47*(2), 191–212. https://doi.org/10.5636/jgg.47.191

Richmond, A. D., Ridley, E. C., & Roble, R. G. (1992). A thermosphere/ionosphere general circulation model with coupled electrodynamics. *Geophysical Research Letters*, *19*(6), 601–604. https://doi.org/10.1029/92gl00401

Rishbeth, H. (2002). Whatever happened to superrotation? *Journal of Atmospheric and Solar-Terrestrial Physics*, *64*(12–14), 1351–1360. https://doi.org/10.1016/s1364-6826(02)00097-4

Rother, M., & Michaelis, I. (2019). *CH-ME-2-PLPT - CHAMP electron density and temperature time series in low time resolution (level 2)*. GFZ Data Services. https://doi.org/10.5880/GFZ.2.3.2019.007

Stolle, C., Manoj, C., Lühr, H., Maus, S., & Alken, P. (2008). Estimating the daytime Equatorial Ionization Anomaly strength from electric field proxies. *Journal of Geophysical Research*, *113*, A09310. https://doi.org/10.1029/2007JA012781

Tao, C., Jin, H., Shinagawa, H., Fujiwara, H., & Miyoshi, Y. (2017). Effect of intrinsic magnetic field decrease on the low- to middle-latitude upper atmosphere dynamics simulated by GAIA: Magnetic field effect on atmospheric dynamics. *Journal of Geophysical Research*, *122*(9), 9751–9762. https://doi.org/10.1002/2017ja024278

Wang, H., & Lühr, H. (2016). Longitudinal variation in zonal winds at subauroral regions: Possible mechanisms. *Journal of Geophysical Research: Space Physics*, *121*, 745–763. https://doi.org/10.1002/2015JA022086

Wang, H., Zhang, K. D., Wan, X., & Lühr, H. (2017). Universal time variation of high-latitude thermospheric disturbance wind in response to a substorm. *Journal of Geophysical Research*, *122*, 4638–4653. https://doi.org/10.1002/2016ja023630

Wang, H., Zheng, Z., Zhang, K., & Wang, W. (2020). Influence of nonmigrating tides and geomagnetic field geometry on the diurnal and longitudinal variations of the equatorial electrojet. *Journal of Geophysical Research: Space Physics*, *125*, e2019JA027631. https://doi.org/10.1029/2019JA027631

Wang, W. B., Talaat, E. R., Burns, A. G., Emery, B., Hsieh, S. Y., Lei, J. H., & Xu, J. Y. (2012). Thermosphere and ionosphere response to subauroral polarization streams (SAPS): Model simulations. *Journal of Geophysical Research: Space Physics*, *117*(A7), A07301. https://doi.org/10.1029/2012JA017656

Weimer, D. R. (2005). Improved ionospheric electrodynamic models and application to calculating Joule heating rates. *Journal of Geophysical Research*, *110*(A5), A05306. https://doi.org/10.1029/2004JA010884

Wharton, L. E., Spencer, N. W., & Mayr, H. G. (1984). The Earth's thermospheric superrotation from Dynamics Explorer 2. *Geophysical Research Letters*, *11*(5), 531–533. https://doi.org/10.1029/gl011i005p00531

Wu, Q., Sheng, C., Wang, W., Noto, J., Kerr, R., McCarthy, M., et al. (2019). The midlatitude thermospheric dynamics from an interhemispheric perspective. *Journal of Geophysical Research: Space Physics*, *124*(10), 7971–7983. https://doi.org/10.1029/2019ja026967

Xiong, C., Lühr, H., & Stolle, C. (2014). Seasonal and latitudinal variations of the electron density nonmigrating tidal spectrum in the topside ionospheric F region as resolved from CHAMP observations. *Journal of Geophysical Research*, *119*, 10416–10425. https://doi.org/10.1002/2014ja020354

Zhang, K., Wang, W., Wang, H., Dang, T., Liu, J., & Wu, Q. (2018). The longitudinal variations of upper thermospheric zonal winds observed by the CHAMP satellite at low and midlatitudes. *Journal of Geophysical Research*, *123*, 9652–9668. https://doi.org/10.1029/2018ja025463